ASCA Measurements of Metallicity and Temperature Distributions in Three Clusters: A4059, MKW 3s and 2A 0335+096

Ken'ichi Kikuchi, Tae Furusho, Hajime Ezawa, Noriko Y. Yamasaki, and Takaya Ohashi

Department of Physics, Tokyo Metropolitan University, 1-1 Minami-Ohsawa,

Hachioji, Tokyo 192-0397

E-mail(KK): kikuchi@phys.metro-u.ac.jp

Yasushi Fukazawa

Department of Physics, University of Tokyo, 7-3-1 Hongo, Bunkyo-ku, Tokyo 113-0033

and

Yasushi Ikebe

Max-Planck-Institut für Extraterrestrische Physik, D-85748, Garching, Germany

(Received; accepted)

Abstract

We present ASCA results on the distributions of metallicity and temperature in 3 bright near-by clusters: A4059, MKW 3s and 2A 0335+096. A significant gradient in the metal abundance is detected in A4059, while other clusters suggest similar gradients with low significance. These features together with recent results on AWM 7 and Perseus clusters suggest that metals injected in the ICM are not effectively mixed in the cluster space. Analysis of the GIS data, without explicitly including the cooling flow model, shows no substantial temperature drop at large radii (at half the virial radii) for the 3 systems. This is contrary to the recent results for 30 clusters by Markevitch et al. (1998) who assume rather strong cooling flows. The gas mass fraction of these clusters are 10–15% within 1 Mpc, which suggests that baryonic fraction of about 20% including the stellar mass is a common level in galaxy groups and clusters.

Key words: Galaxies: abundances — Galaxies: clustering — Galaxies: intergalactic medium — X-Rays: spectra

1. Introduction

Metallicity and temperature distributions in the hot intracluster medium (ICM) in clusters of galaxies provide important information about the history of cluster evolution and galaxy formation. The heating of ICM is supposed to occur via gravitational energy release, compression, and mergers over cosmological time scale. Therefore, temperature distribution reflects various physical conditions in the ICM (strength of shocks, thermal conductivity, magnetic field etc.) as well as cosmological parameters. Recent observations, in particular from ASCA (Tanaka et al. 1994), show non-radial and radial temperature structures in a number of clusters. Among them, Markevitch et al. (1998) report that, when the radius is scaled by the virial radius, the observed 30 clusters reveal a very similar temperature profile.

Metals in the ICM are thought to be injected from individual galaxies. Proportionality between the mass of Fe in the ICM and the total stellar mass in early-type galaxies provides a strong support to this view (Tsuru 1992; Arnaud et al. 1992). However, it is still unclear how metals have been injected into the cluster space. One scenario predicts fast enrichment through galactic winds in the galaxy formation period, and the other important process is a ram-pressure stripping of the galaxy gas over a long time scale. Correct determinations of the total amount of metals and its spatial distribution in relation to those of galaxies and dark matter are useful in determining the scenario of metal injection, which leads to an understanding of the process of chemical evolution of galaxies.

This paper reports ASCA results on metallicity and temperature distributions in 3 cD clusters: A4059, MKW 3s and 2A 0335+096. These clusters are located at a distance of z=0.035-0.049 and fit in the field of view of the GIS. Their temperatures are lower than 4 keV, therefore strong Fe emission line is expected. A4059 is associated with a radio source PKS 2354-35 as a cD galaxy (Schwartz et al. 1991) at z=0.0487, showing an average ICM temperature $kT \approx 3.5$ keV (David et al. 1993). ROSAT (Trümper 1983) has carried out detailed observations of this cluster with PSPC and HRI (Huang and Sarazin 1998). Although the HRI surface brightness profile indicates a strong cooling flow with $\dot{M} \approx 184 M_{\odot} \text{ yr}^{-1}$, the PSPC does not show the spectral signature of the cooling flow with $\dot{M} < 80 M_{\odot} \text{ yr}^{-1}$. The implied \dot{M} is also different from the PSPC deprojection results of $\dot{M} \approx 115 M_{\odot} \text{ yr}^{-1}$ by Allen and Fabian (1997). Temperature structure is derived by Markevitch et al. (1998) based on the analysis assuming a strong cooling flow. Preliminary ASCA results on this cluster are given in Ohashi (1995), in which treatment of the energy dependent point-spread function (PSF) is somewhat premature.

MKW 3s is a poor cluster at z = 0.045 with an average temperature $kT \approx 3.7$ keV (David et al. 1993). Deprojection

analysis of ROSAT PSPC data shows a cooling flow rate of $\dot{M} \approx 161 M_{\odot} \ \rm yr^{-1}$ (Allen and Fabian 1997). Markevitch et al. (1998) report a possible temperature decline with radius based on ASCA data. 2A 0335+096 is also a strong cooling flow cluster at z=0.035 and $kT\approx 3.0$ keV (David et al. 1993). Irwin and Sarazin (1995) report that the cooling flow rate takes a peak of $\dot{M}=400\ M_{\odot}\ \rm yr^{-1}$ at r=60 kpc and remains the same at larger radius. An extra absorbing matter associated with the cluster is significantly seen inside a radius of 500 kpc. Sarazin et al. (1995) reports high-resolution radio structures in the cluster core.

These clusters are thought to be relaxed systems from their smooth morphology and are useful in finding common properties of the ICM in low temperature clusters. The circular structure enables a simple analysis for the profiles, and the handling of stray light and energy-dependent PSF of the ASCA X-ray telescope (XRT) is relatively easy. We investigate distributions of metallicity and temperature in the three clusters of galaxies by taking into account the complex properties of the XRT. We assume $H_0 = 50 \text{ km s}^{-1} \text{ Mpc}^{-1}$ and $q_0 = 0.5 \text{ throughout the paper}$, therefore an angular separation of 1' corresponds to 78 kpc in A4059, 76 kpc in MKW 3s and 59 kpc in 2A 0335+096. The 1 solar number abundance of Fe relative to H is taken as 4.68×10^{-5} (Anders & Grevesse 1989).

2. ASCA Observations and Data Reduction

Table 1 shows the log of ASCA observations. We select the GIS data with a cut-off rigidity > 8 GeV c⁻¹ and the telescope elevation angle from the Earth rim $> 5^{\circ}$ (see Ohashi et al. 1996 and Makishima et al. 1996 for the details of the GIS system). Flare-like events due to the background fluctuation and data taken with unstable attitude are discarded (Ikebe 1995). The non X-ray and the diffuse X-ray background is estimated from the archival data taken during 1993–1994 (Ikebe 1995). Since all targets were observed during 1993–1994, the slow increase of the non X-ray background of the GIS by $\sim 5\%$ yr⁻¹ (Ishisaki et al. 1997, ASCA News No. 4, 26) can be neglected.

Since the X-ray surface brightness of the 3 clusters drops below 50% of the background at 20' radius from the center, the stray light, which are X-rays coming from outside of the field of view, can be ignored. This paper mainly presents GIS results, since it covers the larger region (r > 1 Mpc from the center) and its detector response has less systematic errors than the SIS system.

3. Radial Profile

3.1. ROSAT PSPC Data

The PSF of the ASCA XRT has a half-power diameter of about 3' (Serlemitsos et al. 1995), which is insufficient to resolve the intense central peaks (less than $\sim 1'$ which corresponds to 70–80 kpc) in these clusters. This situation is similar to that we found in Hydra-A cluster (Ikebe et al. 1997). We, therefore, use the ROSAT PSPC image as the model of the surface brightness profile as has been done in Markevitch et al. (1996) and in Ikebe et al. (1997).

The ROSAT PSPC observed A4059, MKW 3s, and 2A 0335+096 on November 21 in 1991, August 15 in 1992, and February 25 in 1991, respectively. We obtained the processed PSPC data from the archival database provided by the ROSAT Scientific Data Center at Max Planck Institut für Extraterrestrische Physik. We exclude contaminating sources in the PSPC data, and correct for the vignetting using EXSAS software package (Zimmermann et al. 1991, EXSAS User's Guide). Figure 1(a), (b) and (c) show the PSPC image of 3 clusters. Assuming the axial symmetry, we fit the radial brightness profiles with a single β model and a constant background, but the model fails to represent the steep profile within $r \lesssim 1'$. Therefore we fit the data with a double β model represented by,

$$I(r) = I_1 \left[1 + \left(\frac{r}{R_{c1}} \right)^2 \right]^{-3\beta_1 + 0.5} + I_2 \left[1 + \left(\frac{r}{R_{c2}} \right)^2 \right]^{-3\beta_2 + 0.5} + \text{constant background}$$
 (1)

Parameters with suffixes 1 and 2 describe the central narrow component and the extended emission, respectively. I_1 and I_2 represent normalization of each component. The data in the radial range of $\sim 20'$ are fitted with this model, without convolving the model with the PSF of the PSPC system (figure 2). We regard that, because of the good angular resolution ($\sim 25''$) of the ROSAT PSPC (Briel et al. 1997, ROSAT User's Handbook), neglecting the effect of PSF dose not cause a problem in making a template profile for the GIS data which has a broader response by a factor of ~ 10 . When the value of β_1 is varied as a free parameter, the PSPC data cannot constrain it because of strong coupling with other parameters. We find that a fixed value of β_1 between 1.0–3.0 gives equally good fit to the PSPC radial profiles for all 3 clusters. Based on this study, we decide to fix β_1 at 1.0 in the following analysis. The center of the X-ray emission is chosen so that the core radius takes the smallest value, i.e. giving the narrowest central profile for each cluster. This method essentially places the center at the peak of the X-ray emission. As summarized in table 2, this model gives a reasonable fit ($\chi^2_{\nu} \lesssim 1.3$) to all clusters. We notice that the narrow component for 2A 0335+096 is extremely strong (as indicated by a large I_1/I_2 value by a factor of ~ 5) compared with other clusters.

3.2. GIS Data

The GIS radial profiles can be described by a single β model because of the poor angular resolution. As shown in the previous section, the PSPC data requires a double β profile in the energy range below 2 keV. The need of the double β profile even in the higher energy range has been shown for Hydra-A cluster based on the joint analysis of PSPC and GIS data (Ikebe et al. 1997). Therefore, we assume a double β model in fitting the GIS data.

To check the consistency between the radial profiles of GIS and PSPC, we fit the GIS data in the energy range 0.7–2 keV with the double β model. The background (non X-ray and cosmic diffuse) is subtracted from the data, and contaminating point sources seen in the PSPC image are masked out. The double β profile, described by the parameter values given in table 2, is convolved with the PSF of the XRT-GIS system. In fitting the GIS data, we choose the center position which minimizes the core radius. The fit is performed over a radius of 0' to 20'. For MKW 3s, we include in the model a foreground soft X-ray emission from the North Polar Spur, which is described in section 4.3. By adjusting the parameters of the wide β component, β_2 and R_{c2} , within the errors of the PSPC fit, an acceptable fit for the 0.7–2 keV GIS data is obtained (table 2). In the later analysis, we fix the parameters of the double β model at the best-fit GIS values as listed in table 2.

4. Spectral Analysis for Individual Annular Regions

4.1. Analysis with an "Isothermal" Model

Examples of the background-subtracted GIS spectra for 3 annular regions are shown in figure 3. One can see a general trend that the equivalent width of Fe-K line decreases from the center to outer region, most clearly in A4059 data. However, this feature is partly flattened due to a flux mixing effect of the XRT as discussed in Ezawa et al. (1997). Because of the extended tail of the PSF of the XRT, the data in each ring are contaminated by photons from near-by rings. In particular, the bright central region causes significant effect to outer rings. Figure 4 shows relative fraction of the contaminating flux from the other region compared with the region's own emission for each ring. The contamination due to the central flux is particularly strong in 2A 0335+096, and is about 40% of the detected flux in the outer ring (r = 7' - 8') originates from the central r < 2' region. The mutual flux contamination between different regions depends on the distributions of surface brightness, temperature and metallicity. This means that a simultaneous fit of the energy spectra in the entire regions in the cluster is the only way to obtain the correct

distributions of temperature and metallicity.

When distributions of temperature and metallicity are uniform within the cluster, we can create the proper response function based only on the surface brightness profile and work out the correct spectral parameters (see Honda et al. 1996). This method, i.e. assuming the uniform spectrum in the calculation of the response function, can be used to carry out the first-order estimation of temperatures in individual regions. We can, at the same time, examine whether this particular model with an isothermal ICM and uniform metallicity is consistent with the data or not. In calculating the response function for 3 clusters, the double β profile determined by the GIS data analysis (table 2) is taken as the template brightness profile. This analysis gives a conservative estimate of temperature variation, if present, in the cluster in the sense that the variation amplitude is suppressed (Honda et al. 1996).

Using the above-described response, we first carried out a joint fit for the GIS and SIS spectra in the inner region (r < 2') where the scattering effect is small. The GIS spectra for the annular regions are then fitted to look at the radial variation of the ICM properties. We use the Raymond-Smith (Raymond & Smith 1977; hereafter R-S) thermal models with XSPEC ver. 9. Temperature (kT) and metal abundance with solar ratio (Z) are varied as free parameters. The models give acceptable fit in most of the regions with $\chi^2/\nu \lesssim 1.3$. Results for individual clusters are described in the following sections.

4.2. A4059

The GIS and SIS pulse-height spectra for the central region (r < 2') of the cluster are jointly fitted first with a single temperature R-S model. The interstellar absorption $N_{\rm H}$ is fixed at the Galactic value of 1.11×10^{20} cm⁻² (Stark et al. 1992). We obtain $\chi^2/\nu = 543/350$, with best-fit parameters kT = 4.0 keV and metal abundance Z = 0.58 solar, respectively. See Table 3 for the errors of the parameters. This fit is poor and the χ^2 value is not formally acceptable at the 90% confidence. Two-temperature model is tried next with separate abundance and common absorption as free parameters. This gives a better fit with $\chi^2/\nu = 500/346$, and the parameter values are listed in Table 3. Assuming a common absorption for the hot and the cool components, the metal abundance of the hot component (kT = 4.2 keV) becomes 0.62 solar and the cool component (0.9 keV) requires very low metallicity. Hwang et al. (1997) showed that the abundance determined by Fe-L and Fe-K lines are almost consistent for a range of plasma temperatures $\sim 2 - 4$ keV, and suggested that the systematic offset between Fe-L and Fe-K abundances was found if one did not consider excess absorption for the cool component. If we carry out the fit with the

same two-temperature model with common metal abundance and separate absorption as free parameters, we obtain $\chi^2/\nu = 498/346$ with the common abundance $0.60^{+0.09}_{-0.08}$ solar, and temperature $4.1^{+0.3}_{-0.2}$ keV and $0.7^{+0.2}_{-0.1}$ keV for the hot and cool components, respectively. The absorption $N_{\rm H}$, assuming z=0 for the absorber, is $7.9^{+0.5}_{-2.0} \times 10^{21}$ cm⁻² and $8.1^{+3.3}_{-4.0} \times 10^{20}$ cm⁻² for the cool and hot components, respectively. Considering the systematic errors of 2–3 $\times 10^{20}$ cm⁻² on the $N_{\rm H}$ due to calibration uncertainty (Dotani et al. 1996, ASCA News No. 4, 3), the absorption for the hot component is almost consistent with the Galactic value.

The annular GIS spectra are then fitted with single temperature R-S models with the $N_{\rm H}$ fixed at the Galactic value. Radial distributions of temperature and metal abundance are shown in figure 5(a-1), (a-2) and table 4. The temperature is almost constant with a peak-to-peak fluctuation less than 0.6 keV. The metal abundance, on the other hand, shows a systematic drop as a function of radius. The central value of $0.75^{+0.14}_{-0.13}$ solar is very high for a cluster, and it drops by a factor of about 3 at r > 10'. This abundance profile is smoother than the actual one because of the PSF effect as mentioned earlier, however it enables us to test whether the abundance variation is significant or not because the correct response for constant temperature and abundance is used in the fit. Taking the 7 values of the temperature and abundance for annular regions and their 1σ confidence limits, we test the constant temperature or constant abundance model with χ^2 method. The fit gives $\chi^2/\nu = 8.1/6$ for the temperature, and 21.1/6 for the abundance, respectively. Therefore, we can conclude that the abundance variation in A4059 is significant at more than 99% confidence, while the temperature is consistent with a constant. If we replace the abundance data in the innermost region with the combined GIS and SIS result (0.62 solar), the abundance variation is still significant at 90% confidence.

4.3. MKW 3s

The spectrum in the central region is examined by jointly fitting the GIS and SIS data within r < 2' with R-S models. As shown in Table 3, the single temperature model with fixed Galactic $N_{\rm H}$ gives a poor fit with $\chi^2/\nu = 506/360$ and the two temperature model gives a better fit with $\chi^2/\nu = 436/357$. Because of strong coupling between spectral parameters, we need to assume a common metal abundance for the hot and cool components in this fit.

The outer region of MKW 3s is significantly contaminated by soft X-ray emission from the North Polar Spur (NPS). We fit the GIS spectrum in a radial range of 12' - 18' with thermal models because the emission from the

NPS is dominant in this region, and find that it can be approximated by 0.28 keV thermal bremsstrahlung with a surface brightness of 1.1×10^{-14} erg cm⁻² s⁻¹ arcmin⁻² in 0.5 - 2.0 keV. This is close to the PSPC flux $(0.8 \times 10^{-14}$ erg cm⁻² s⁻¹ arcmin⁻²) measured in the same sky region with the *ROSAT* All Sky Survey (Snowden et al. 1995). The NPS flux in 0.5 - 10 keV is about 30% of the cluster emission for the same solid angle at r = 10' from the cluster center. Therefore, we include this component in fitting all the data of MKW 3s. Apart from this complexity in the foreground emission, the cluster emission is described by a single temperature R-S model in all regions. As indicated in figure 5(b-1), the temperature does not vary significantly with the radius. The metal abundance in this cluster shows a smaller gradient than in A4059. The average value is about 0.35 solar within 4', and it drops to 0.2 -0.3 solar at r > 8'. Again, we test the constant temperature/abundance models in the same way as for A4059, and the χ^2 fits show that no significant variation in temperature or abundance is present in MKW3s at 90% confidence.

4.4. 2A 0335+096

A strong cool component with $kT \sim 1$ keV and an excess $N_{\rm H} \sim 1 \times 10^{21}$ cm⁻² are detected in the central region (r < 3') of this cluster with the PSPC (Irwin and Sarazin 1995). A single-temperature R-S fit to the combined GIS and SIS spectra in r < 2' shows that the model is unacceptable with $\chi^2/\nu = 831/448$ (see Table 3). The single-temperature fit is unacceptable even if we take the GIS data only. A 2-temperature model with separate metal abundance gives a better fit to with $\chi^2/\nu = 582/445$ for the combined GIS and SIS data. Both components show similar abundance values as shown in Table 3. To better model the very strong cool component, we include variable metal abundances (vR-S) for the cool component. This model is used to avoid the problems arising from calibration uncertainties and inappropriate modeling of atomic physics (see Fabian et al. 1994) in the spectral fit. Figure 6 shows the SIS and GIS spectra fitted with the model. Free parameters in the fit are 2 normalizations, 2 temperatures, single $N_{\rm H}$ common to the 2 components, and 6 abundances (5 for the cool and 1 for the hot component, respectively). The fit is acceptable with the best-fit parameters as shown in table 5 with $\chi^2/\nu = 511/440$. The low Mg abundance is probably caused by incorrect modeling of Fe-L lines near the Mg-K lines (Fabian et al. 1994). The $N_{\rm H}$ value of 3.0×10^{21} cm⁻² is greater than the Galactic one (1.7×10^{21} cm⁻², Stark et al. 1992), which is consistent with the PSPC measurement by Irwin and Sarazin (1995). When $N_{\rm H}$ is fixed at the Galactic value, GIS spectral fit gives consistent spectral parameters as shown in table 5.

Assuming the two temperature component in all regions, we fit the GIS spectra for the annular regions. A common

 $N_{\rm H}$ value for the hot and cool components is fixed at the level of PSPC measurement given in Irwin and Sarazin (1995). Also, temperature and abundance of the cool component are fixed at those in table 5, so the spectral shape of the cool component is not varied during the fit. This treatment is necessary because GIS is rather insensitive to the spectral features below ~ 1 keV. As a result, free parameters in the fit are temperature, abundance and normalization of the hot component, and normalization of the cool component. Spectra in the outer regions (r > 4') can be approximated by a single temperature R-S model. In the outer regions, the single and two-temperature models give the difference of only 10% in the hot-component temperature.

The resultant values in Table 5 are tested against the constant model, and we find that the abundance can be consistent at 90% confidence but that the temperature variation is significant at 99% confidence. It seems, however, likely that the 2 temperature model is not good enough to model the strong complex emission at the center of this cluster.

5. Analysis with Image Response Matrix

5.1. Analysis Method

In the previous section, we found a strong indication of the abundance decline with radius in A4059. To evaluate the true values of temperature and abundance, we need to jointly fit the spectra in the annular regions using the image response matrix (Ikebe et al. 1997; Markevitch et al. 1996).

The analysis with the "isothermal" model in the previous section only gives an approximate solution of temperature and metal abundance. When contribution of the stray light can be ignored, the combined fit of the spectral data is performed by making so-called "image response matrix" as described in detail in Ikebe et al. (1997) and in Markevitch et al. (1996). Here, we will follow these approach and evaluate true distributions of temperature and metal abundance.

In this analysis, the data format we deal with is a set of spatially sorted spectra rather than energy sorted images. This preserves our sensitivity to variations of temperature and metal abundance. The spectral data of a cluster are jointly tested against a certain model whose spatial distribution is described by a β -model. We numerically construct 3-dimensional model clusters and predict GIS spectra by convolving the sky image through image response matrices. For all clusters, the GIS data are divided into 3 concentric regions and are fitted simultaneously.

5.2. A4059

Since the spectral fit for individual annular regions in the previous section indicates that the ICM is isothermal, we will assume a constant temperature for all regions and only look into the variations of metal abundance. In calculating a 3-dimensional model cluster, the volume emissivity is described by,

$$\epsilon(r) = n_{\text{gas}}^2(r)\Lambda(T, Z(r)), \tag{2}$$

where $\Lambda(T, Z(r))$ denotes the cooling function with metal abundance Z. The hot gas distribution in the 3-dimensional space is approximated as,

$$n_{\text{gas}}^{2}(r) = n_{0}^{2} \left[\frac{I_{1}}{I_{1} + I_{2}} \left\{ 1 + \left(\frac{r}{R_{c1}} \right)^{2} \right\}^{-3\beta_{1}} + \frac{I_{2}}{I_{1} + I_{2}} \left\{ 1 + \left(\frac{r}{R_{c2}} \right)^{2} \right\}^{-3\beta_{2}} \right], \tag{3}$$

where n_0 denotes central density of the hot gas, and I_1 , I_2 , R_{c1} , R_{c2} , β_1 , and β_2 are 2-dimensional double β -model parameters in table 2.

A model with constant temperature and constant metal abundance is examined in the first place. For the 3 annular regions (r=0'-2', 2'-7' and 7'-18'), we fit the data in the energy range 0.7–10 keV with a single temperature R-S model. Systematic error of the image response matrix is included in χ^2 value by adding 3% of the model flux (Ikebe et al. 1998). This fit is acceptable with the minimum χ^2 value of 482.4 for $\nu=452$, with kT=4.08(3.97-4.19) keV and Z=0.42(0.37-0.48) solar. As shown in section 4.2 significant variation in the metal abundance exists in this cluster, with the temperature consistent with a constant. The purpose of the analysis in this section is to estimate the true radial profile of the metal abundance based on the joint fit of the annular spectra.

Using the image response matrix, we fit the 3 annular spectra by varying the metal abundances in 3 regions separately. Free parameters are the central density n_0 , the common temperature kT, and 3 metal abundances for the 3 regions. The best fit χ^2 value is 428.8 for $\nu = 450$: a better fit than the constant abundance model. Radial variation of the metal abundance is shown in figure 7(a), and the correlation of metal abundances in the 3 regions are shown in figure 8, which show 90% and 99% confidence contours for metal abundances for combinations of 2 different regions. The figure shows that the abundances in the inner region and the outer region are different with more than 99% confidence.

5.3. MKW 3s

Again, the ICM can be assumed to have a single temperature R-S spectrum from the previous analysis. We assume different metal abundances for 3 regions. A 0.28 keV thermal bremsstrahlung is added for the North Polar Spur, and its normalization (N_{brems}) is varied in each region. Therefore, free parameters are the central density $n_{0,\text{hot}}$, the temperature kT, 3 metal abundances (Z), and 3 normalizations (N_{brems}) for the 3 regions. The abundance results are shown in figure 7(b). The best-fit points suggest abundance gradient with $\chi^2 = 482.9$ with $\nu = 439$. However, models with constant metal abundances for the energy range of 5.5–7.5 keV gives $\chi^2 = 19.6$ for $\nu = 13$, which is also acceptable. Therefore, we cannot exclude the constant abundance model for this cluster.

5.4. 2A 0335+096

The spectral fit for individual regions shows gradients in both temperature and metallicity, so this is included in the combined spectral fit. We also found the strong cool component concentrated in the central region. Since it is difficult to determine the spatial distribution of the cool component with ASCA as mentioned before, we assume that the distribution of the cool component is the same as that of the narrow β -model,

$$n_{\text{gas,cool}}^2(r) = n_{0,\text{cool}}^2 \left[1 + \left(\frac{r}{R_{c1}} \right)^2 \right]^{-3\beta_1}$$
 (4)

with the parameters fixed at the values listed in table 2. The volume emissivity is given as,

$$\epsilon(r) = f(r) \left[n_{\text{gas,hot}}^2(r) \Lambda(T_{\text{hot}}(r), Z_{\text{hot}}(r)) + n_{\text{gas,cool}}^2(r) \Lambda(T_{\text{cool}}, Z_{\text{cool}}) \right], \tag{5}$$

where, we assume that $n_{\text{gas,hot}}^2$ has a double β distribution as described in equation (3). Since this model gives a radial profile which is a sum of a double β (hot) and a single β (cool) models, we introduce a correction factor f(r) to adjust the emissivity profile to a double β distribution as seen in the PSPC data. The actual value of f(r) is 0.6-1.1 within r < 20'. The parameter n_{gas} differs from the true gas density, partly because of the correction factor f(r). Also, the present attempt in which the projected emission is simply divided into the 2 independent hot and cool components would inevitably result in a systematic deviation in the estimated value of n_{gas} from the correct one.

Then we fit the 3 regions simultaneously, with free parameters $n_{0,\text{hot}}$, $n_{0,\text{cool}}$, 3 temperatures, and 3 abundances. The fixed parameters and their values are the same as those in the individual spectral fit described in section 4.4. The results of the spectral fits are shown in figure 7(c-1) and (c-2) for the temperature of the hot component and

the metal abundance, respectively. The fit is acceptable with $\chi^2 = 562.4$ with $\nu = 592$. Constant metal abundance gives an acceptable fit to the data in the energy range 5.5–7.5 keV, with $\chi^2 = 18.2$ for $\nu = 20$. Therefore, we cannot exclude the constant abundance model as well as in MKW 3s. When we assume a step function with a radius of 2' for the surface brightness distribution of the cool component, the temperature and abundance of the hot component vary by less than 10%.

6. Mass Profile

Based on the best fit model obtained in section 5, we calculate an integrated mass distribution of the hot gas $(M_{\rm gas})$ and the total gravitating mass $(M_{\rm total})$. In calculating $M_{\rm gas}$, we neglect the cool component and only include the hot component since emission mechanism of the cool component very likely involves different physics than the gravitational heating (see Fabian 1994, Makishima 1996, Ikebe et al. 1997). The double β profile with the parameters shown in table 2 with a constant temperature of 4.1 keV, 3.6 keV and 3.2 keV for A4059, MKW 3s and 2A 0335+096, respectively, are assumed. The abundance gradient is approximated by a smooth function and included for A4059. The results are shown in table 6 and in figure 9.

Spherical symmetry and hydrostatic equilibrium are assumed in estimating M_{total} . Again, presence of the cool component is ignored. Since the constant temperature given above is also assumed, the gravitating mass is given by $M_{\text{total}}(r) = -(kTr/\mu G m_{\text{H}})(d \ln n/d \ln r)$. The same double β profile for the hot component is used as that in the calculation of M_{gas} . As shown in table 6 and in figure 9, the resultant mass profiles indicate that the gas mass occupies 10 - 15% of the gravitating mass within 1 Mpc for all 3 clusters.

7. Discussion

ASCA observations have detected an abundance gradient in the cluster of galaxies, A 4059. The feature is significant at 90% confidence when we take into account the effect of ASCA PSF.

Following the detection of metallicity gradient in clusters of galaxies with Ginga and Einstein (White III et al. 1994), recent studies show non-uniformity in the metallicity distribution in two radial scales. One is the small-scale ($\lesssim 100~\rm kpc$) central excess, often associated with the cool component around cD galaxies. This feature is seen in Centaurus cluster (Ikebe et al. 1998), Hydra A (Ikebe et al. 1997), Virgo cluster (Matsumoto et al. 1996), A262 (David et al. 1996), and AWM 7 (Xu et al. 1997). Excess metals are probably supplied by the cD galaxy and trapped

in the deep potential well. We found that total iron mass within 100 kpc is about $1.2 \times 10^9 M_{\odot}$ for A4059. Since the B band magnitude of PKS 2354-35, cD galaxy of A4059, is 13.90 (Green et al. 1990), the iron mass-to-light ratio around the cD is about $0.004 M_{\odot}/L_{\odot}$ for A4059. This value is almost the same as the average for clusters (= $0.01 - 0.02 M_{\odot}/L_{\odot}$, Arimoto et al. 1997). Therefore, the excess iron at the center of A4059 is within a range which the cD galaxy can possibly supply.

The other finding is a large-scale gradient in the metal abundance (over 500 kpc) which is now detected in 2 cD clusters; AWM 7 (Ezawa et al. 1997) and Perseus cluster (Ezawa 1998). It is likely that the metals injected from individual galaxies are not effectively mixed in the ICM and holds the original galaxy distribution, as indicated from various models (e.g. Metzler and Evrard 1994). This feature would be common to other clusters, but very few clusters have been studied from ASCA with enough sensitivity to the outer region (r > 500 kpc). A rather uniform abundance distribution is found within central 200 kpc of the non-cD cluster A1060 (Tamura et al. 1996), which may be different from the cD systems.

From the present result of A4059, we cannot definitely say whether the high metallicity is only associated with the cD galaxy or it is extended. Although the radial distribution of the metal abundance suggests some large-scale gradient, more observations with better statistics or better angular resolution is certainly necessary. As shown in figure 7, 2A 0335+098 and MKW 3s also suggest some gradient in the radial metallicity distribution, but we cannot reject the case of spatially uniform abundance. Therefore, present results have strengthened the possibility that the abundance gradient is a common feature in many cD clusters.

Relation between cooling flows and metallicity gradient is discussed by Fujita and Kodama (1995) and by Allen and Fabian (1998). Fujita and Kodama show that cooling flows with a mass deposition rate $\dot{M} \gtrsim 100~\rm M_{\odot}~\rm yr^{-1}$ tends to make the abundance distribution flatter because the flow compresses the distribution pattern. This effect is probably compensated by the large metal supply from the cD galaxy. Allen and Fabian (1998) shows that cooling flow clusters have an average metallicity higher than that of non cooling flow systems by a factor of ~ 1.8 . They discuss that the central region of high metallicity is not mixed by mergers in cooling flow clusters. Based on the results on metallicity distribution so far measured with ASCA, we consider it is highly likely that all the cD clusters (usually reported to accompany strong cooling flows) have a sharp concentration of metals in their centers. On the other hand, the large scale gradient over ~ 500 kpc is probably unrelated to either cD galaxy or cooling flows and rather common to all clusters which have not experienced recent mergers.

One impact of the abundance gradient is its effect on the estimated total mass of Fe ($M_{\rm Fe}$). Because of the n^2 dependence of the X-ray emissivity, a small amount of Fe concentrated in the center can emit strong Fe-K line in the overall spectrum. If we approximate the abundance gradient in A4059 by a smooth exponential function with Z=1.0 solar at the center declining to 0.20 solar at r=1 Mpc, then $M_{\rm Fe}$ is estimated to be $2.7\times10^{10}M_{\odot}$ in r<1 Mpc. The total Fe mass inferred from the abundance gradient model is about 70 % of that indicated if the abundance were uniform at $Z\approx0.45$ solar.

Markevitch et al. (1998) recently revealed temperature profiles in about 30 clusters. The temperature drops by a factor of 2 at half the virial radius. Approximating the virial radius by r_{180} , in which the mean mass density is 180 times the critical density, and using the formula given by Markevitch et al. (1998) as $r_{180} = 1.95h^{-1}(T_x/10\text{keV})^{1/2}$ Mpc, r_{180} for the 3 clusters are 2.5 Mpc (32') for A4059, 2.3 Mpc (30') for MKW 3s and 2.2 Mpc (37') for 2A 0335+096. We note from figure 5 and 7 that only A4059 shows a hint of temperature drop by less than 20% at $r = 0.5r_{180}$. Other clusters show no sign of temperature drop, and 2A 0335+096 indicates a temperature rise in the outer region. Part of this feature may be due to an exceptionally strong cool component in the center. Even though 2 clusters, A4059 and MKW 3s, are in the sample of Markevitch et al. (1998), the results are significantly different.

The most likely cause of the difference is the treatment of cooling flows. Markevitch et al. (1998) assumes cooling flow models in the central region, while we simply fit the data with single temperature models. Adding a cool component $(kT \sim 1 \text{ keV})$ raises the temperature of the "hot" component so that the average central temperature is kept nearly constant. The GIS instrument is rather insensitive to the cool component, so our analysis here is inevitably simplified to some extent. On the other hand, Huang and Sarazin (1998) note that the PSPC data of A4059 do not show spectral signature of the cooling flow with $\dot{M} < 80 M_{\odot} \text{ yr}^{-1}$ and discuss a possibility that the gas may be "young" so that the cooling has not yet established itself. Ikebe et al. (1997) show that the strong central peak in the X-ray emission of Hydra-A cluster is dominated by hot $(kT \sim 4 \text{ keV})$ component rather than cool one, and discuss that the cooling flow rate is 10 times less than the previous estimation. These results indicate that a straightforward inclusion of the cooling flow models tends to result in an overestimation of the amount of cool gas (hence overestimation of the hot-gas temperature in the center). We therefore suspect that the true temperature profile would be somewhere between the present result and the Markevitch et al. (1998) one. Close examination of temperatures in the very outer regions of near-by clusters, which should be less affected by the scattering effect of the XRT, would bring more definite conclusions than the present sample. Also, joint analysis of the PSPC and

ASCA data in the central region would be interesting to know the nature of the cool emission and the potential profile.

All three clusters indicate that the fraction of $M_{\rm gas}$ is 10–15% of the total mass within r < 1 Mpc. It may be because these clusters have the similar size and temperature. However, similar values of the gas fraction have been reported in various clusters (see Briel et al. 1992; Henry et al. 1993; Elbaz et al. 1995; David 1997). This suggests that the baryonic fraction of about 20%, including the few % stellar mass occupying a few % of the gravitational mass, is a common number in groups and clusters. The constancy over a large range of cluster richness may suggest that it is a cosmic average (therefore, $\Omega_B/\Omega \sim 0.2$) as discussed by White et al. (1993). We need to point out, however, that clusters occupy only a few % of the volume of the local universe and much of the space has so far been unexplored.

In the mass calculation we assume an isothermal temperature distribution. If there is a radial drop of the temperature (in this case a strong cool component has to be present in the cluster center), the mass estimation at large radii ($r \sim 1$ Mpc) is affected in the following manner. In the standard formula to describe the mass under a hydrostatic equilibrium (e.g. Sarazin 1988, p. 178), the term kTr is reduced to 70–80% of the isothermal value based on the comparison of Markevitch et al. (1998) value and the present ones at $r \sim 1$ Mpc. The term $d \ln T/d \ln r$ changes from 0 to about 0.5 if we assume the average temperature profile in Markevitch et al. (1998). The two terms give opposite effect on the total mass and it changes by only about 10%. Therefore, our mass estimation is unlikely to be seriously wrong.

We would like to thank the ASCA Team for spacecraft operation and data acquisition. We also thank Dr. T. Tamura and Dr. S. Sasaki for important comments. K. K. acknowledges support from the Japan Society for the Promotion of Science for Young Scientists. This work is partly supported by the Grants-in Aid of the Ministry of Education, Science, Sports and Culture of Japan, 08404010.

References

Allen S.W., Fabian A.C. 1997, MNRAS 286, 583

Allen S.W., Fabian A.C. 1998, MNRAS 297, 63

Anders E., Grevesse N. 1989, Geochim. Cosmochim. Acta 53, 197

Arimoto N., Matsushita K., Ishimaru Y., Ohashi T., Renzini A. 1997, ApJ 477, 128

Arnaud M., Rothenflug R., Boulade O., Vigroux L., Vangioni-Flam E. 1992, A&A 254, 49

Briel U.G., Henry J.P., Böhringer H. 1992, A&A 259, 31

David L.P., Slyz A., Jones C., Forman W., Vrtilek S.D., Arnaud K.A. 1993, ApJ 412, 479

David L.P., Jones C., Forman W. 1996, ApJ 473, 692

David L.P. 1997, ApJL 484, 11

Elbaz D., Arnaud M., Böhringer H. 1995, A&A 293, 337

Ezawa H., Fukazawa Y., Makishima K., Ohashi T., Takahara F., Xu H., Yamasaki N.Y. 1997, ApJ 490, L33

Ezawa H. 1998, Ph.D. thesis, Univ. of Tokyo

Fabian A.C., Arnaud K.A., Bautz M.W., Tawara Y. 1994, ApJL 436, 63.

Fabian A.C. 1994, ARA&A 32, 227

Fujita Y., Kodama H. 1995, ApJ 452, 177

Green M.R., Godwin J.G., Peach J.V. 1990, MNRAS 243, 159

Henry J.P., Briel U.G., Nulsen P.E.J. 1993, A&A 271, 413

Honda H., Hirayama M., Watanabe M., Kunieda H., Tawara Y., Yamashita K., Ohashi T., Hughes J.P., Henry J.P. 1996, ApJ 473, L71

Huang Z., Sarazin C.L. 1998, ApJ 496, 728

Hwang U., Mushotzky R.F., Loewenstein M., Markert T.H., Fukazawa, Y., Matsumoto, H. 1997, ApJ 476, 560

Ikebe Y. 1995, Ph.D. thesis, Univ. of Tokyo

Ikebe Y., Makishima K., Ezawa H., Fukazawa Y., Hirayama M., Honda H., Ishisaki Y., Kikuchi K. et al. 1997, ApJ 481, 660

Ikebe Y., Makishima K., Fukazawa Y., Tamura T., Xu H., Ohashi T., Matsushita K. et al. 1998, ApJ submitted

Irwin J.A., Sarazin C.L. 1995, ApJ 455, 497

Makishima K., Tashiro M., Ebisawa K., Ezawa H., Fukazawa Y., Gunji S., Hirayama M., Idesawa E. et al. 1996, PASJ 48, 171

Makishima K. 1996, in X-Ray Imaging and Spectroscopy of Cosmic Hot Plasmas, ed F. Makino & K. Mitsuda (Universal Academy Press, Tokyo) p137

Markevitch M., Mushotzky R., Inoue H., Yamashita K., Furuzawa A., Tawara Y. 1996, ApJ 456, 437

Markevitch M., Forman W.R., Sarazin C.L., Vikhlinin A. 1998, ApJ 503, 77

Matsumoto H., Koyama K., Awaki H., Tomida H., Tsuru T., Mushotzky R., Hatsukade I. 1996, PASJ 48, 201

Metzler C.A., Evrard A.E. 1994, ApJ 437, 564

Ohashi T. 1995, in Dark Matter, ed S. S. Holt & C. L. Bennett (AIP, New York) p255

Ohashi T., Ebisawa K., Fukazawa Y., Hiyoshi K., Horii M., Ikebe Y., Ikeda H., Inoue H. et al. 1996, PASJ 48, 157

Raymond J.C., Smith B.W. 1977, ApJS 35, 419

Sarazin C.L., Baum S.A., O'Dea C.P. 1995, ApJ 451, 125

Schwartz D.A., Bradt H.V., Remillard R.A., Tuohy I.R. 1991, ApJ 376, 424

Serlemitsos P.J., Jalota L., Soong Y., Kunieda H., Tawara Y., Tsusaka Y., Suzuki H., Sakima Y. et al. 1995, PASJ 47, 105

Snowden S.L., Freyberg M.J., Plucinsky P.P., Schmitt J.H.M.M., Trümper J., Voges W., Edgar R.J., McCammon D., Sanders W.T. 1995, ApJ 454, 643

Stark A.A., Gammie C.F., Wilson R.W., Bally J., Linke R.A., Heiles C., Hurwitz M. 1992, ApJS 79, 77

Tamura T., Day C.S., Fukazawa Y., Hatsukade I., Ikebe Y., Makishima K., Mushotzky R.F., Ohashi T., Takenaka K., Yamashita K. 1996, PASJ 48, 671

Tanaka Y., Inoue H., Holt S.S. 1994, PASJ 46, L37

Trümper J. 1983, Adv. Space Res. 2, 241

Tsuru T. 1992, Ph.D. thesis, Univ. of Tokyo

White III R.E., Day C.S.R., Hatsukade I., Hughes J.P. 1994, ApJ 433, 583

White S.D.M., Navarro J.F., Evrard A.E., Frenk C.S. 1993, Nature 366, 429

Xu H., Ezawa H., Fukazawa Y., Kikuchi K., Makishima K., Ohashi T., Tamura T. 1997, PASJ 49, 9

Table 1. ASCA observation \log of the 3 clusters

Target	Pointing (J2000.0)*	Observed Date (UT)	Exposure (sec) [†]
A4059	$23^{\rm h}57^{\rm m}20^{\rm s}.4,-34^{\rm d}43^{\rm m}10^{\rm s}$	1994/07/03	34151
MKW 3s	$15^{\rm h}21^{\rm m}28^{\rm s}.9,+07^{\rm d}42^{\rm m}36^{\rm s}$	1993/08/02	29258
2A 0335+096	$03^{\rm h}38^{\rm m}45^{\rm s}.2,+10^{\rm d}06^{\rm m}18^{\rm s}$	1994/08/22	40185

 $[\]ast$ Center position of the GIS2 field of view.

 $[\]dagger$ Total exposure time of the GIS2 and 3 after the data screening described in section 2.

19

Table 2. Result of fitting the radial profiles of PSPC and GIS with a double β model. Errors represent the 90% confidence limit for one parameter. For the GIS, parameters of the narrow component and normalization ratio (I_1/I_2) are fixed to the best-fit values derived by the PSPC.

	Narrow	component	Extended of	component		
Target	eta_1	$R_{ m c1}$	eta_2	$R_{ m c2}$	I_1/I_2	χ^2/ν
(Detector)		[arcmin]		[arcmin]		
A4059						
(PSPC)	1.00	0.67	0.59	1.48	1.49	88.34/67
	(fixed)	(0.43-1.45)	(0.57 – 0.67)	(1.23 - 3.28)	(0.25 – 2.29)	
(GIS)	1.00	0.67	0.61	1.53	1.49	16.15/14
	(fixed)	(fixed)	(0.59 – 0.63)	(1.36-1.71)	(fixed)	
MKW 3s						
(PSPC)	1.00	0.76	0.61	1.35	1.43	76.69/74
	(fixed)	(0.51 – 1.02)	(0.58 – 0.65)	(1.05 – 1.89)	(0.64-2.21)	
(GIS)	1.00	0.76	0.63	1.35	1.43	12.59/10
	(fixed)	(fixed)	(0.59 – 0.67)	(1.06 – 1.57)	(fixed)	
2A 0335+096						
(PSPC)	1.00	0.93	0.64	1.93	8.10	88.34/74
	(fixed)	(0.88 – 0.97)	(0.61 – 0.67)	(1.62 – 2.25)	(6.35 - 10.72)	
(GIS)	1.00	0.93	0.64	1.50	8.10	17.07/14
	(fixed)	(fixed)	(0.62 – 0.66)	(1.27 – 1.64)	(fixed)	

Table 3. Result of the simultaneous spectral fitting of GIS and SIS for the central 2' region. Errors represent the 90% confidence limit for one parameter.

Target		A4059	MKW3s	2A 0335+096
Single R-S	kT	4.0	3.7	2.7
	(keV)	(3.8-4.1)	(3.6 – 3.8)	(2.6-2.8)
	Z	0.58	0.49	0.71
	(solar)	(0.50 – 0.66)	(0.43 – 0.56)	(0.66-0.77)
	χ^2/ν	543.4/350	506.4/360	831.4/448
Double R-S	kT_1	0.9	1.4	1.3
	(keV)	(0.8 – 1.2)	(1.0 – 2.0)	(1.2-1.4)
	Z_1	0.04	0.42	0.63
	(solar)	(< 0.12)	(0.35 – 0.49)	(0.46 – 1.01)
	kT_2	4.2	3.9	3.3
	(keV)	(3.9 – 4.9)	(3.0 – 5.8)	(3.0 – 3.7)
	Z_2	0.62	0.42	0.55
	(solar)	(0.53 – 0.67)	(fixed to Z_1)	(0.47 – 0.64)
	χ^2/ u	500.0/346	436.6/357	581.8/444

Table 4. Spectral fitting results with "Isothermal" models. Errors represent the 90% confidence limit for one parameter.

Target	radius	$kT \; (\mathrm{keV})$	Z (solar)	χ^2/ν
A4059	0' - 2'	3.83 (3.68–3.99)	$0.75\ (0.62 – 0.89)$	134.8/129
	2'-4'	4.14 (4.00–4.30)	$0.45\ (0.35 – 0.53)$	173.5/129
	4'-6'	4.07 (3.88–4.27)	$0.40\ (0.300.51)$	73.0/62
	6' - 8'	3.91 (3.67–4.16)	$0.48\ (0.33 – 0.64)$	86.0/62
	8' - 10'	3.97 (3.63–4.36)	$0.25\ (0.08 – 0.44)$	25.1/31
	10' - 14'	3.83 (3.44–4.31)	$0.22\ (0.02 - 0.45)$	35.2/30
	14' - 18'	$3.51\ (2.97 – 4.30)$	$0.71\ (0.20 - 1.47)$	32.0/30
MKW 3s	0' - 2'	3.59 (3.42–3.77)	0.31 (0.22–0.41)	142.0/128
	2'-4'	3.56 (3.42–3.72)	0.38 (0.29–0.48)	140.5/128
	4'-6'	$3.44\ (3.27 – 3.65)$	$0.34\ (0.23 - 0.46)$	56.7/61
	6' - 8'	3.37 (3.10–3.67)	$0.17\ (0.04 – 0.31)$	53.0/61
	8' - 12'	3.41 (3.09–3.79)	$0.21\ (0.05 - 0.40)$	30.0/30
	12' - 18'	3.65 (3.06–4.49)	0.13 (0.00–0.44)	34.0/30
2A 0335+096	0' - 2'	3.38 (3.28–3.48)	0.52 (0.44-0.62)	159.0/126
	2'-4'	3.26 (3.09–3.45)	$0.42\ (0.35 - 0.50)$	189.4/128
	4'-6'	3.51 (3.26–3.81)	$0.37\ (0.29 - 0.46)$	122.7/128
	6' - 8'	3.08 (2.97–3.30)	$0.49\ (0.38 - 0.60)$	65.4/61
	8' - 10'	3.63 (3.14–4.43)	$0.35\ (0.19 - 0.52)$	49.5/61
	10' - 14'	$4.73\ (4.07 – 5.81)$	0.33 (0.18–0.48)	25.3/29
	14' - 18'	4.79 (4.09–6.70)	0.21 (0.00-0.43)	34.2/29

NOTE: Interstellar absorption $(N_{\rm H})$ is fixed to the Galactic value, $1.11\times10^{20}~{\rm cm^{-2}}$ for A4059, and $2.88\times10^{20}~{\rm cm^{-2}}$ for MKW 3s. For 2A 0335+096, we fixed $N_{\rm H}$ at the sum of the Galactic and the excess absorption measured by the PSPC (Irwin & Sarazin 1995): $3.03\times10^{21}~{\rm cm^{-2}}$, $2.40\times10^{21}~{\rm cm^{-2}}$, $2.20\times10^{21}~{\rm cm^{-2}}$ and $1.72\times10^{21}~{\rm cm^{-2}}$ for the region of 0'-2', 2'-4', 4'-8' and 8'-18', respectively.

Table 5. Result of the spectral fit for the central 2' region of 2A 0335+096 with a 2 temperature model.

(- 0)		
Cool component (vR-S)		
Temperature (keV)	1.42(1.35-1.6)	65)
Abundance (solar)		
He, C, N	1.0 (fixed)	
O, Ne	1.36(0.28 - 2.9)	91)
${ m Mg}$	0.00(<0.09)	
Si	0.91(0.64-1.8)	58)
S, Ar, Ca	0.27(0.03 - 0.4)	48)
Fe, Ni	0.69(0.52-1.5)	12)
Hot component (R-S)		
Temperature (keV)	3.48(3.10-4.5)	27)
Abundance (solar)	0.54(0.46 - 0.6)	65)
$N_{ m H}~({ m cm}~ imes 10^{21})$	3.03(2.79 - 3.5)	27)
χ^2/ν	510.7/440	

Table 6. Integrated mass of the hot gas and the total gravitating matter.

Target	Average temperature	Gas mass $(M_{\rm gas})$	Gravitating mass (M_{total})
	$[\mathrm{keV}]$	$(< 1 \mathrm{\ Mpc}) \ [M_{\odot}]$	$(< 1 \mathrm{\ Mpc}) \ [M_{\odot}]$
A4059	4.1	3.3×10^{13}	2.6×10^{14}
MKW 3s	3.6	3.4×10^{13}	2.4×10^{14}
2A 0335+096	3.2	3.1×10^{13}	2.1×10^{14}

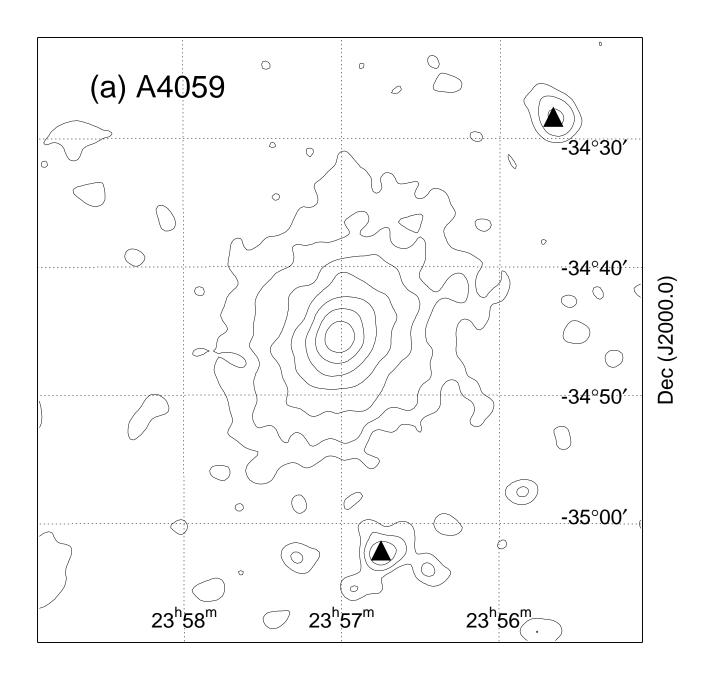
Fig. 1. Contour plot of the PSPC image in the 0.4–2.0 keV band for (a) A4059, (b) MKW 3s and (c) 2A 0335+096.

These images are convolved with a Gaussian of 0'.5 FWHM. The contour levels are logarithmic scale with a step size of factor of 2. The positions excluded from the analysis due to contaminating sources are indicated by triangles.

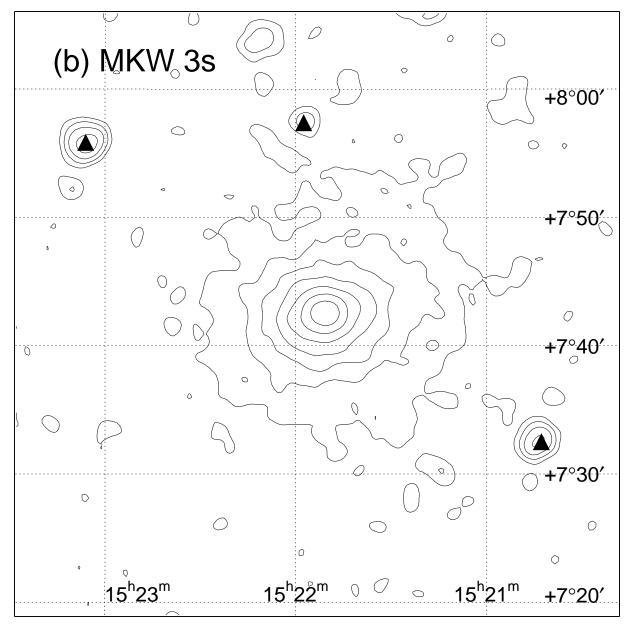
- Fig. 2. PSPC radial profiles fitted with the double β models. (a) A4059, (b) MKW 3s and (c) 2A 0335+096. The data (open circles) gives the X-ray surface brightness in the energy band of 0.7–2 keV. Dashed curves show narrow β component, dotted curves show extended one, and the constant background is indicated by the solid line.
- Fig. 3. Background-subtracted energy spectra for 3 concentric annular regions obtained with GIS. (a) A4059, (b) MKW 3s and (c) 2A 0335+096. Each cluster shows a general trend that the equivalent width of Fe K line (~6-7 keV) decreases from the center to outer region.
- Fig. 4. Simulation result of the contaminating flux from the annular sky regions to individual regions of the GIS for (a) A4059, (b) MKW 3s and (c) 2A0335+096. The horizontal axis shows the radius ranges of the GIS, and vertical axis shows the fraction of photons originated in different sky regions. We assume that the intensity profile of each cluster is represented by double β model with the parameter values shown in Table 3.
- Fig. 5. Results from the GIS spectral fit with the "Isothermal" model: (a-1) temperature of A4059, (a-2) abundance of A4059, (b-1) temperature of MKW 3s, (b-2) abundance of MKW 3s, (c-1) temperature of 2A0335+096 and (c-2) abundance of 2A0335+096. Error bars represent the 90% confidence level for a single interesting parameter. Diamonds show results for broad binning in the radial direction.
- Fig. 6. The top panel shows the SIS and GIS spectrum of 2A 0335+096 in the central 2' region, and the bottom one indicates the deviation of the data in the form of χ . Crosses represents the data, and the solid line shows the 2 temperature model summarized in Table 4.
- Fig. 7. Results from the GIS spectral fit with the image response matrix method described in section 4. The 4 panels show (a) abundance of A4059, (b) abundance of MKW 3s, (c-1) temperature of 2A 0335+096 and (c-2) abundance of 2A 0335+096, respectively. Error bars are the 90% confidence level for a single interesting parameter. A Smooth exponential curve is fitted to the results in (a).

Fig. 8. Confidence contour for the metal abundances in 2 different annular regions in A4059. The inner and the outer contours correspond to 90% and 99% limits for 2 parameters. The solid straight line indicates the case for the same abundance.

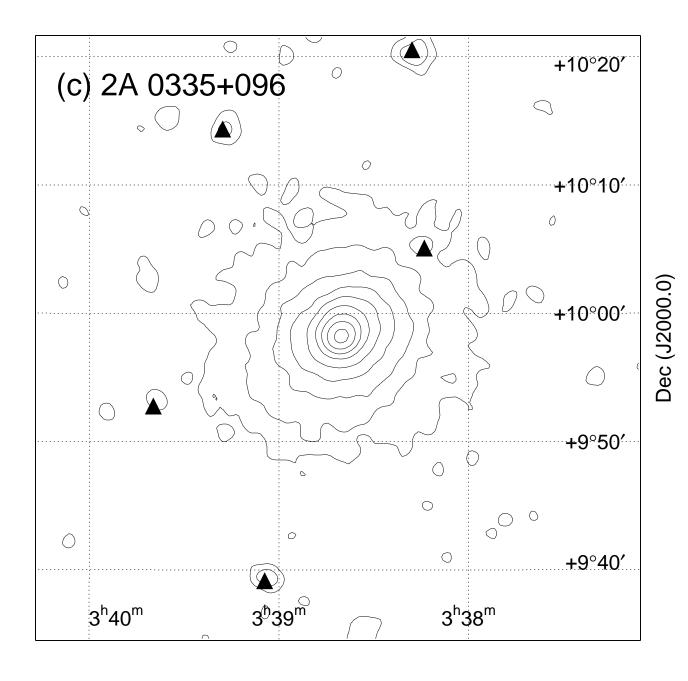
Fig. 9. Integrated mass profile of ICM $(M_{\rm gas})$ and total gravitating mass $(M_{\rm total})$ as a function of distance from the center for (a) A4059, (b) MKW 3s and (c) 2A 0335+096. The gas fraction $(M_{\rm gas}/M_{\rm total})$ is also indicated in the bottom panels.



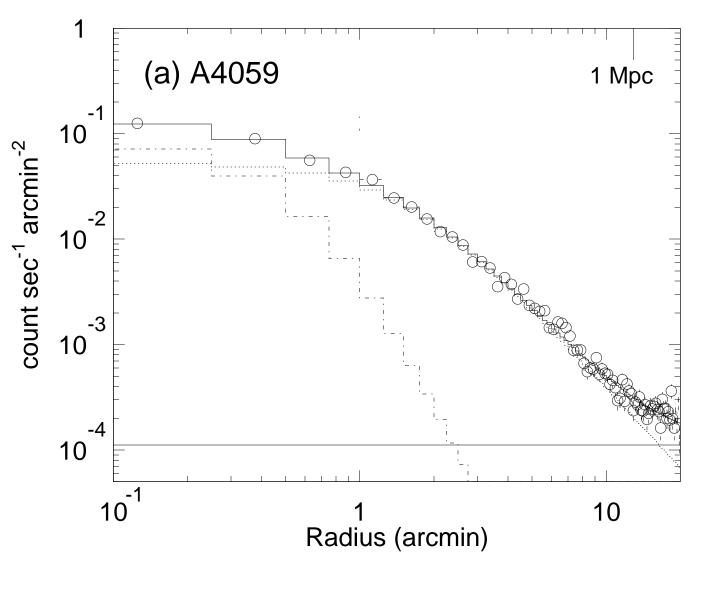
RA (J2000.0)

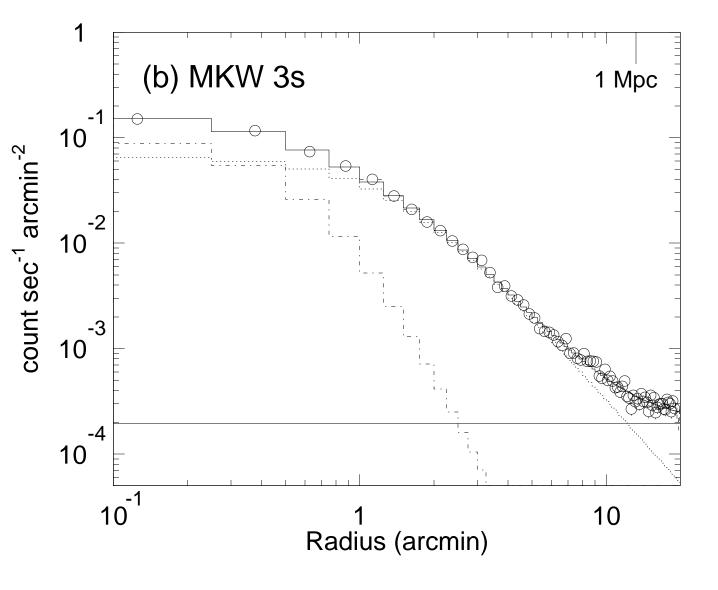


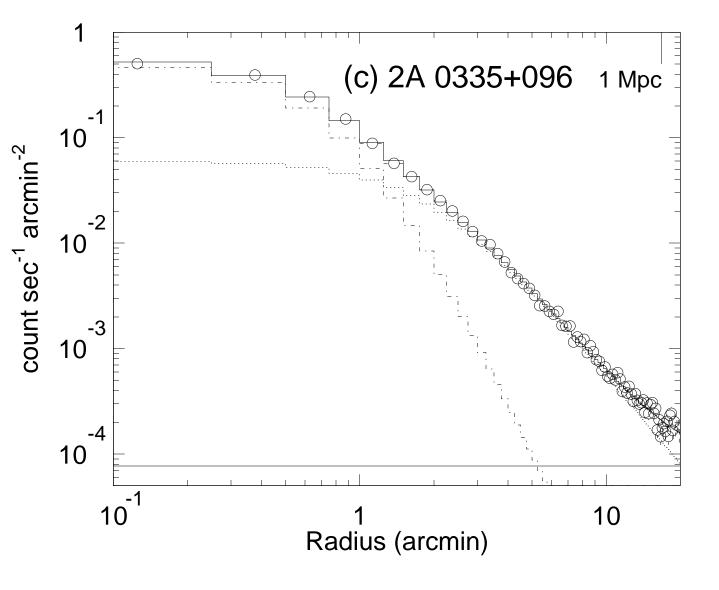
RA (J2000.0)

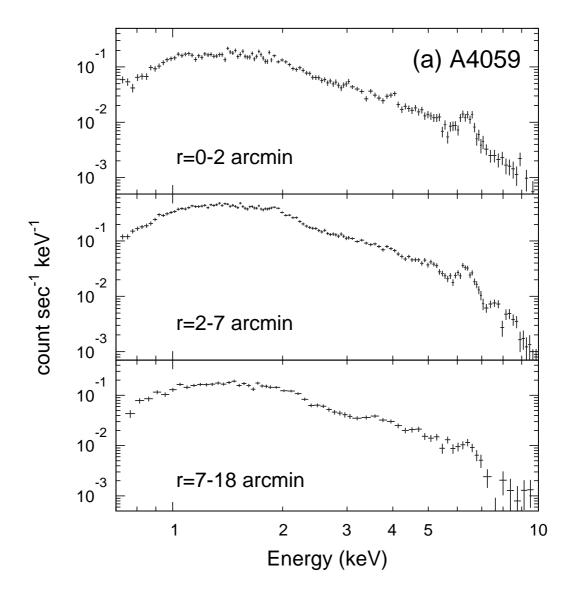


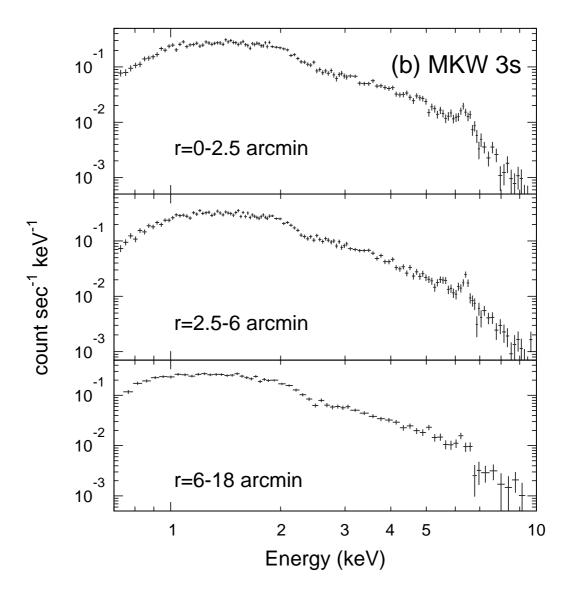
RA (J2000.0)

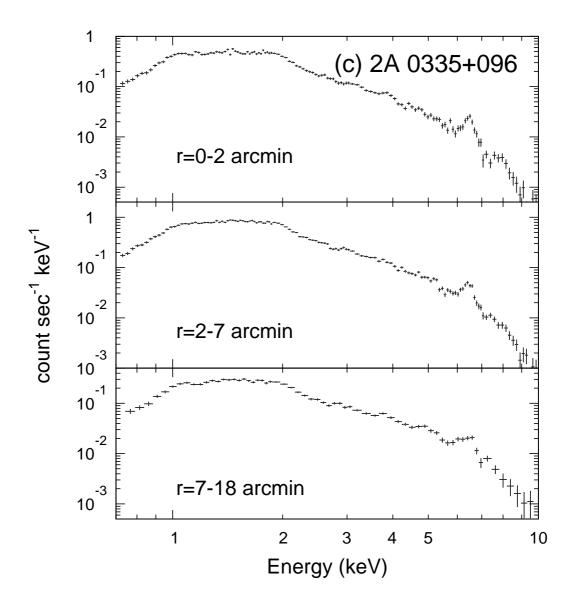


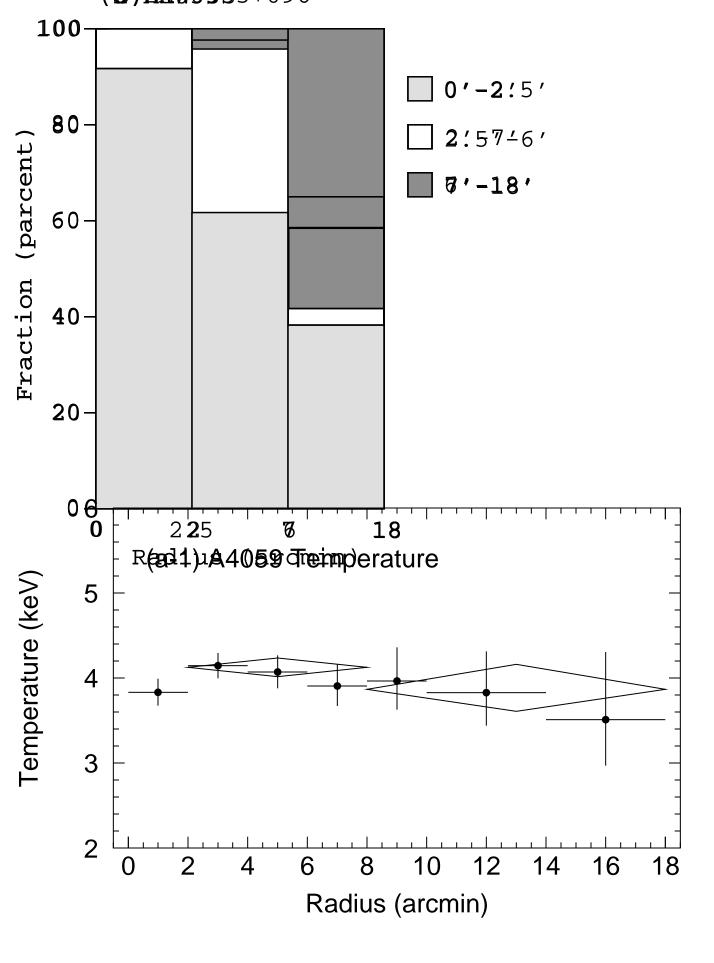


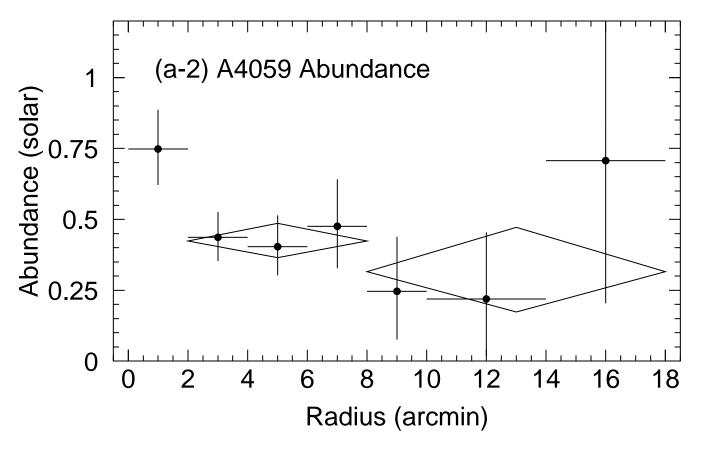


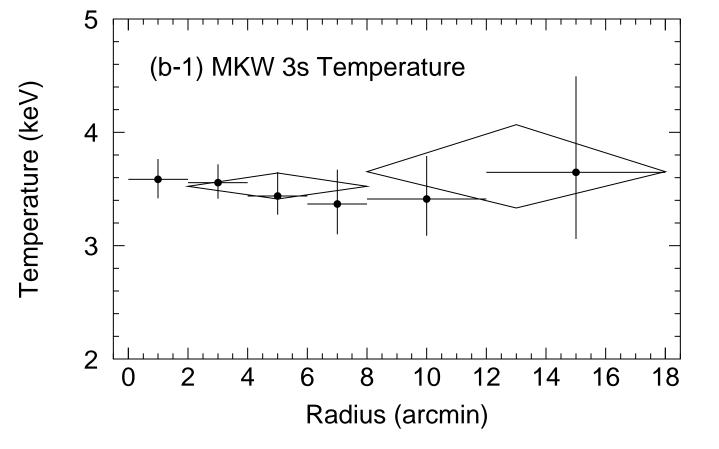


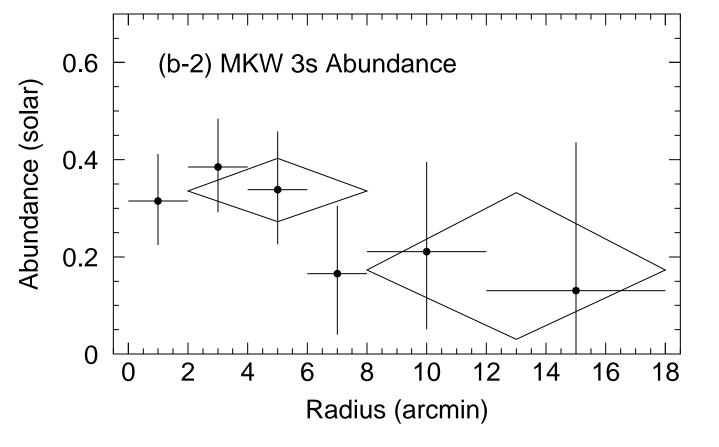


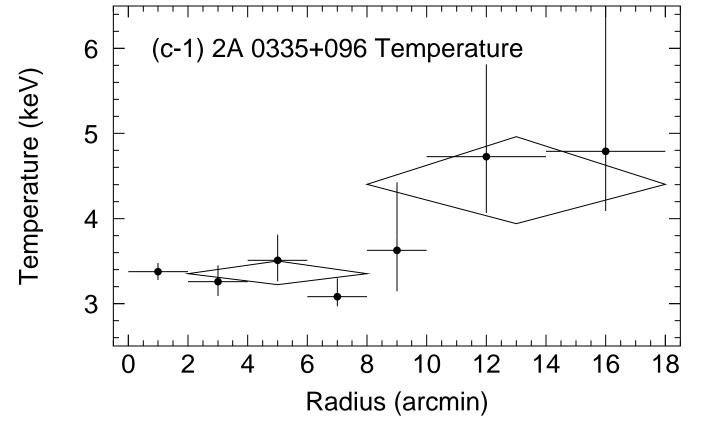


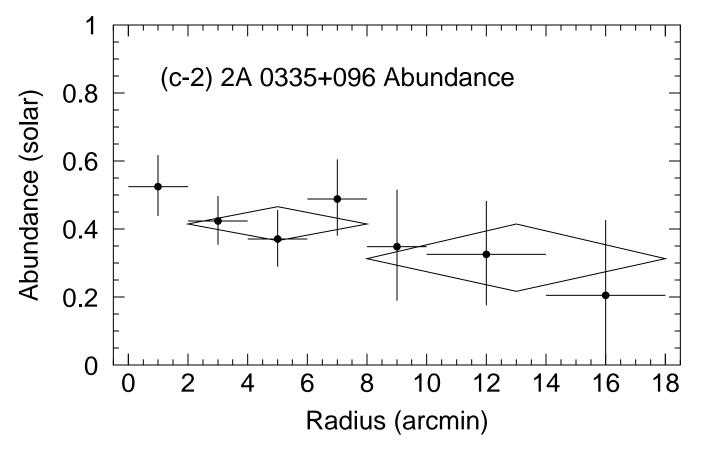












-4-2 0 2 4 10 ⁻³ 0.01 0.1 1
Energy (keV)

